

Article

A Temperature-Compensation Technique for Improving Resolver Accuracy

Wandee Petchmaneelumka , Vanchai Riewruja *, Kanoknuch Songsuwankit and Apinai Rerkratn

School of Engineering, King Mongkut's Institute of Technology Ladkrabang, Ladkrabang, Bangkok 10520, Thailand; wandee.pe@kmitl.ac.th (W.P.); kanoknuch.so@kmitl.ac.th (K.S.); apinai.re@kmitl.ac.th (A.R.)

* Correspondence: vanchai.ri@kmitl.ac.th

Abstract: Variation in the ambient temperature deteriorates the accuracy of a resolver. In this paper, a temperature-compensation technique is introduced to improve resolver accuracy. The ambient temperature causes deviations in the resolver signal; therefore, the disturbed signal is investigated through the change in current in the primary winding of the resolver. For the proposed technique, the primary winding of the resolver is driven by a class-AB output stage of an operational amplifier (opamp), where the primary winding current forms part of the supply current of the opamp. The opamp supply-current sensing technique is used to extract the primary winding current. The error of the resolver signal due to temperature variations is directly evaluated from the supply current of the opamp. Therefore, the proposed technique does not require a temperature-sensitive device. Using the proposed technique, the error of the resolver signal when the ambient temperature increases to 70 °C can be minimized from 1.463% without temperature compensation to 0.017% with temperature compensation. The performance of the proposed technique is discussed in detail and is confirmed by experimental implementation using commercial devices. The results show that the proposed circuit can compensate for wide variations in ambient temperature.



Citation: Petchmaneelumka, W.; Riewruja, V.; Songsuwankit, K.; Rerkratn, A. A Temperature-Compensation Technique for Improving Resolver Accuracy. *Sensors* **2021**, *21*, 6069. <https://doi.org/10.3390/s21186069>

Academic Editor: Marco Carratu

Received: 6 August 2021

Accepted: 8 September 2021

Published: 10 September 2021

Publisher's Note: MDPI stays neutral with regard to jurisdictional claims in published maps and institutional affiliations.



Copyright: © 2021 by the authors. Licensee MDPI, Basel, Switzerland. This article is an open access article distributed under the terms and conditions of the Creative Commons Attribution (CC BY) license (<https://creativecommons.org/licenses/by/4.0/>).

Keywords: resolver; inductive transducer; temperature-compensation technique; subtract-and-sum circuit; opamp

1. Introduction

A resolver, which is a kind of inductive transducer, is a useful device in instrumentation and measurement systems. The operation of a resolver is identical to a variable transformer, which consists of a primary winding as a rotor and two secondary windings placed at right angles from each other as stators [1–4]. Resolvers are widely used for the measurements of the angle, position, and speed in instrumentation and control systems. Resolvers provide high reliability, durability, and resolution. Therefore, resolvers are especially suitable for harsh environments. Resolvers have been applied in industries, military equipment, robots, aerospace, radars, electric vehicles, and medical and scientific equipment [5–7]. Practically, the primary winding of a resolver is excited by a sinusoidal signal. The resolver signals from the two secondary windings known as the quadrature signals are proportional to the sine and cosine functions of the rotor shaft angle, which are in the form of amplitude modulation with a suppressed carrier. Traditionally, a synchronous demodulator based on an analog multiplier, low-pass filter, or analog switch and integrator has been used to extract the shaft-angle signals from the resolver signals [1,8–10]. However, the response time and accuracy of these demodulators deteriorate due to the large time constant and phase shift caused by the dominant pole of the low-pass filter and integrator. To overcome these disadvantages, an alternative technique using a peak-amplitude finder was introduced [3,11,12]. This technique provides a simple configuration and rapid response. Recently, techniques for determining position from a resolver signal in digital form have been proposed in the literature [5,13–17]. Unfortunately, these approaches require the resolver to operate at a constant ambient temperature to achieve this accurately.

Many parameters can affect the accuracy of the resolver, such as phase shifts between the primary winding and secondary windings, amplitude imbalance and imperfect quadrature between two resolver signals, and variation in the ambient temperature [1,3,18]. Amplitude imbalance and imperfect quadrature cause errors in the determination of the shaft angle. Recently, a technique to minimize the error of the shaft-angle determination caused by amplitude imbalance and imperfect quadrature was proposed [18]. However, this technique requires a high-speed processor. Consequently, a complex measurement system structure is required. An amplitude imbalance or phase shift between the primary and secondary winding can be prevented using a technique proposed in the literature [3]. Variation in the ambient temperature influences the resistance of the winding, the mutual inductance, the magnetizing current, and the core loss current of the resolver, causing amplitude error in the resolver signals. The traditional technique to minimize this temperature effect is based on the use of an inverse tangent of the ratio of two resolver signals [1,4,8]. However, the disadvantage of this technique is that a large error occurs when the resolver signal is close or equal to zero. The response time is also rather slow for this technique. An approach based on the use of a temperature-sensitive device was developed to compensate for the temperature effect of inductive transducers [19–22]. The temperature effect in the technique mentioned above is compensated for in an open-loop procedure, which causes inaccuracies in the resolver signal. Other techniques are based on the modification of the transducer's structure or material to obtain low-temperature sensitivity [23–25], and the use of reference inductance to compensate for the temperature effect [26]. The authors of [27] constructed a closed-loop technique to compensate for the temperature of the inductive transducer without using a temperature sensor. This technique requires the output signals of the transducer to be in linear form, which is only suitable for transducers used for the measurement of linear displacement, such as linear variable differential transformers (LVDTs). In contrast, the resolver signals are in the sine and cosine functions. Therefore, the techniques mentioned above are not applicable to these resolvers.

The purpose of this study was to construct a temperature-compensation technique for a resolver without requiring a temperature-sensitive device. From the transformer principle, the parameters of the secondary winding side can be referred to the primary winding side [28]. Therefore, the error of the resolver signal on the secondary winding side because of temperature can be extracted from the primary winding side. In this study, the error in the resolver signal due to the temperature effect was investigated from the current flowing through the primary winding of the resolver using the opamp supply-current-sensing technique [29–31]. The amplitude variation in the resolver signal due to the temperature effect was determined and compensated for using subtract-and-sum topology. The performance of the proposed technique was analyzed and confirmed by experimental implementation. All the devices used in the proposed technique are commercially available. Hence, the attractions of the proposed technique are its performance, simple configuration, and low cost.

2. Principle

The principle of the resolver is shown in Figure 1 [1]. A sinusoidal signal $v_{ex} = V_P \sin(\omega_{ex}t)$ is applied to the primary winding L_P , where V_P is the peak amplitude voltage, $\omega_{ex} = 2\pi f_{ex}$ is the angular frequency, and f_{ex} is the frequency of the excitation signal. Two secondary windings are terminated by the load resistors $R_{L1} = R_{L2}$, and the resolver signals v_{S1} and v_{S2} are produced in form of quadrature sinusoidal signals as

$$v_{S1} = k_{RS}v_{ex} \sin(\theta_S) = k_{RS}V_P \sin(\omega_{ex}t) \sin(\theta_S) \quad (1)$$

$$v_{S2} = k_{RS}v_{ex} \cos(\theta_S) = k_{RS}V_P \sin(\omega_{ex}t) \cos(\theta_S) \quad (2)$$

where k_{RS} denotes the transformation ratio of the resolver and θ_S is the shaft angle. Practically, the amplitude of the resolver signals is affected by variations in the ambient temperature because the mutual inductance, the resistance of both the primary and secondary

windings, the magnetizing current, and the core loss current of the resolver depend on variations in the ambient temperature.

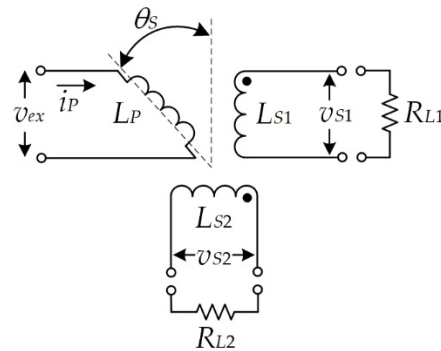


Figure 1. Principle of the functioning of the resolver.

Therefore, the transformation ratio k_{RS} is affected by the ambient temperature. The resolver signals from Equations (1) and (2) can be written as

$$v_{S1} = k_{RS}(1 - \alpha\Delta T)V_P \sin(\omega_{ex}t) \sin(\theta_S) \quad (3)$$

$$v_{S2} = k_{RS}(1 - \alpha\Delta T)V_P \sin(\omega_{ex}t) \cos(\theta_S) \quad (4)$$

where α and ΔT are the temperature coefficient of the resolver and the temperature deviation from room temperature at 25 °C, respectively. From Equations (3) and (4), $\sin(\omega_{ex}t)$ can be simply removed by a synchronous demodulator. Thus, the resolver signals can be expressed as

$$v_{S1} = k_{RS}(1 - \alpha\Delta T)V_P \sin(\theta_S) \quad (5)$$

$$v_{S2} = k_{RS}(1 - \alpha\Delta T)V_P \cos(\theta_S) \quad (6)$$

The amplitude of the resolver signals depends on variation in the ambient temperature. The variation in the ambient temperature affects all the quantities of the resolver and causes deviation in the transformation ratio k_{RS} . Based on the principle on which transformers function, the secondary winding currents flowing through the load resistors R_{L1} and R_{L2} can be referred to the primary side [28]. Therefore, the primary winding current i_p can be used to investigate the secondary winding current. The disturbance of the primary winding current i_p (which includes the magnetizing current and the core loss current) by the ambient temperature can be approximated as

$$i_p = \frac{(1 - \alpha\Delta T)v_{ex}}{|Z_{PL}|} = (1 - \alpha\Delta T)k_R v_{ex} \quad (7)$$

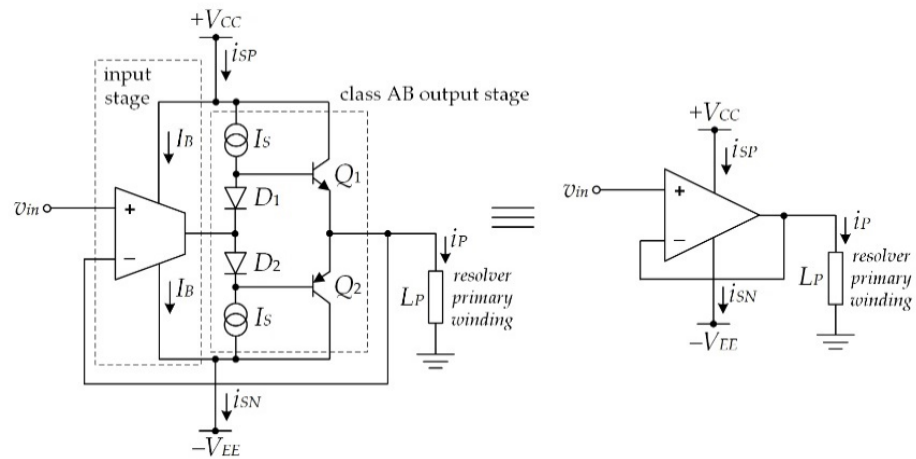
where $k_R = 1/|Z_{PL}|$, and Z_{PL} is the combination of the primary-side impedance and the secondary-side impedance referred to the primary side of the resolver. It should be noted that the changes in the magnetizing current and the core loss current due to temperature are very small compared to the change in the secondary winding current, which can be considered as negligible [25,32]. If the temperature effect on the primary winding current is compensated for, then the secondary winding current is compensated simultaneously. Practically, the primary winding L_P of the resolver is driven by the opamp, as shown in Figure 2a. From Figure 2a, the output state of the opamp is generally a class-AB configuration where the output current of the opamp exists within its supply current. In this study, a bipolar opamp was used for experimental implementation. From Figure 2a, the supply currents i_{SP} and i_{SN} of the opamp can be expressed as [29–31]

$$i_{SP} = I_B + \frac{\sqrt{(i_p^2 + 4I_S^2)} + i_p}{2} \quad \text{for } |i_p| < 2I_S \quad (8)$$

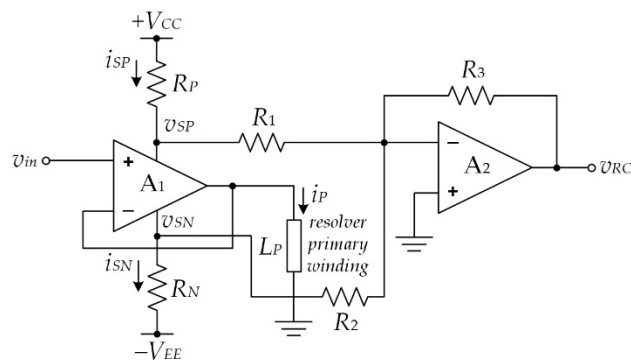
and

$$i_{SN} = I_B + \frac{\sqrt{(i_P^2 + 4I_S^2)} - i_P}{2} \text{ for } |i_P| < 2I_S \tag{9}$$

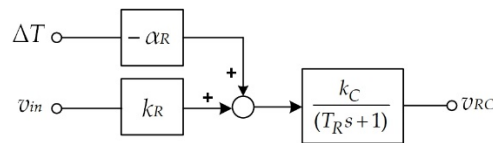
where I_B and I_S denote the quiescent current and the bias current of the class-AB output state of the opamp, respectively.



(a)



(b)



(c)

Figure 2. (a) Opamp equivalent circuit; (b) opamp supply-current sensing technique; (c) block diagram of primary winding current extraction including the temperature effect.

For the large-amplitude primary winding current i_P or $|i_P| > 2I_S$, the currents i_{SP} and i_{SN} can be described by

$$i_{SP} = \begin{cases} I_B + i_P & \text{for } i_P > 2I_S \\ I_B & \text{for } i_P < -2I_S \end{cases} \tag{10}$$

and

$$i_{SN} = \begin{cases} I_B & \text{for } i_P > 2I_S \\ I_B + i_P & \text{for } i_P < -2I_S \end{cases} \tag{11}$$

The primary winding current i_p of a resolver affected by temperature can be observed from the supply current of the opamp. The schematic diagram used to achieve the supply current of the opamp is shown in Figure 2b. From the circuit in Figure 2b, if the input signal v_{ex} is applied, then the primary winding current i_p can be described by v_{ex}/Z_{PL} . The resistors R_P and R_N convert the current signals i_{SP} and i_{SN} to the voltage signals v_{SP} and v_{SN} , respectively. Opamp A_2 and the resistors R_1 , R_2 , and R_3 function as a summing amplifier to sum the voltage signals v_{SP} and v_{SN} [30,31]. Thus, the primary winding current i_p of the resolver is determined in the form of the voltage signal v_{RC} . The voltage signal v_{RC} can be stated as

$$v_{RC} = \frac{R_P R_3}{R_1} i_{SP} + \frac{R_N R_3}{R_2} i_{SN} \quad (12)$$

Practically, the resistances $R_1 = R_2$ and $R_P = R_N$ are assigned. If the peak amplitude of the current signal i_p is greater than $2I_S$ or $|i_p| > 2I_S$, then Equation (12) can be written as

$$v_{RC} = \frac{R_P R_3}{R_1} i_p = (1 - \alpha \Delta T) k_C k_R v_{in} \quad (13)$$

The primary winding current of the resolver can be determined from the voltage signal v_{RC} . Practically, the parameter k_C is normally assigned as $1/k_R$. The simulation result of the circuit depicted in Figure 2b obtained using the PSPICE analog simulation program is shown in Figure 3, where a sinusoidal signal of 3 kHz with a peak amplitude of 2V is applied as the input signal v_{in} . The parameters of the primary winding L_P were measured and modeled from the resolver used in this study. From Figure 3, the phase lag θ_P occurs between the excitation signal v_{in} and the signal v_{RC} due to the behavior of the resolver. Therefore, the resolver behavior can be approximated by a single-pole expression as

$$\frac{v_{RC}(s)}{v_{in}(s)} = \frac{(1 - \alpha \Delta T) k_C k_R}{(T_R s + 1)} \quad (14)$$

for

$$T_R = \frac{\tan \theta_P}{\omega_{ex}}$$

where T_R is the time constant of the resolver. From Equation (14), the circuit in Figure 2b affected by temperature can be represented by the block diagram shown in Figure 2c, where $\alpha_R = \alpha k_R$.

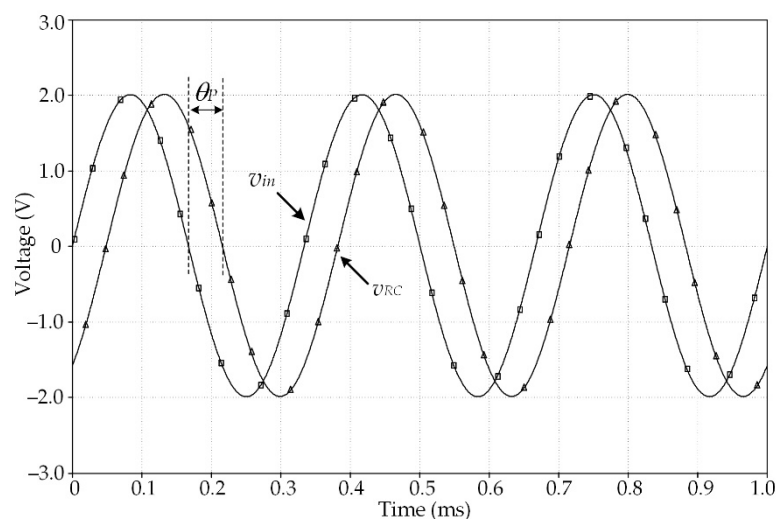


Figure 3. Simulation result of Figure 2b.

3. Temperature-Compensation Technique

A simple closed-loop configuration to compensate for the temperature effect is shown in Figure 4a, where the subtract-and-sum topology is depicted within the dashed-line frame. The phase-lead compensator in Figure 4a is required to compensate for the phase lag θ_P of the resolver's behavior. Therefore, the time constant T_l of the phase-lead network is set to equal the time constant T_R for the in-phase condition between the signals v_F and v_{in} . From Figure 4a, the closed loop transfer function can be stated as

$$v_F(s) = \frac{(1 + k_P)\gamma k_C k_F k_R}{(1 + \gamma k_C k_F k_P k_R) \left(1 + \frac{\gamma T_l s}{(1 + \gamma k_C k_F k_P k_R)}\right)} v_{in}(s) - \frac{\gamma \alpha_R k_C k_F k_R}{(1 + \gamma k_C k_F k_P k_R) \left(1 + \frac{\gamma T_l s}{(1 + \gamma k_C k_F k_P k_R)}\right)} \Delta T \quad (15)$$

where k_P and k_F are the proportional gain and the compensation gain, respectively, and γ is the attenuation factor of the phase-lead compensator. Normally, $k_C = 1/k_R$ and $k_F = 1/\gamma$ are assigned. If $k_P \gg 1$ and $\gamma k_C k_F k_P k_R \gg 1$, then Equation (15) can be expressed as

$$v_F(s) = \left(v_{in}(s) - \frac{\alpha_R}{k_P} \Delta T \right) \frac{1}{\left(1 + \frac{\gamma T_l s}{k_P}\right)} \quad (16)$$

From Equation (16), the magnitude of the signal v_F for $v_{in} = V_P \sin(\omega_{ex} t)$ can be approximated as

$$|v_F(j\omega)| = \left(V_P - \frac{\alpha_R}{k_P} \Delta T \right) \left[\frac{1}{\sqrt{\left(1 + \left(\frac{\gamma T_l \omega_{ex}}{k_P}\right)^2\right)}} \right] \quad (17)$$

From Equation (17), the parameters of $\gamma = 0.1$, $T_l = 67.63 \mu\text{s}$, and $\omega_{ex} = 18.85 \text{ krad/s}$ were achieved from experimental implementation. Thus, the denominator of the terms in the square brackets in Equation (17) can be approximated as 1. It is evident that the temperature effect of the primary winding current i_P on the resolver can be minimized by increasing the gain value k_P . The proposed circuit for the block diagram in Figure 4a is shown in Figure 4b. The block diagram of the sum-and-subtract topology in the dashed-line frame in Figure 4a can be replaced by the dashed-line block SS_1 in Figure 4b to minimize the active device used for the experimental implementation.

The proposed circuit consists of three opamps as active devices. The operation of the proposed circuit can be explained as follows: from Figure 4b, the opamp A_1 and resistors R_{f1} and R_{f2} function following the sum-and-subtract scheme to obtain the error signal between the input signal v_{in} and the feedback signal v_F . The capacitance C_C is employed to avoid unstable sum-and-subtract scheme operation [27]. For a small value of the capacitance C_C , the output signal v_{ex} of the opamp A_1 can be stated as

$$v_{ex} = v_{in} + \frac{R_{f2}}{R_{f1}} (v_{in} - v_F) = v_{in} + k_P (v_{in} - v_F) \quad (18)$$

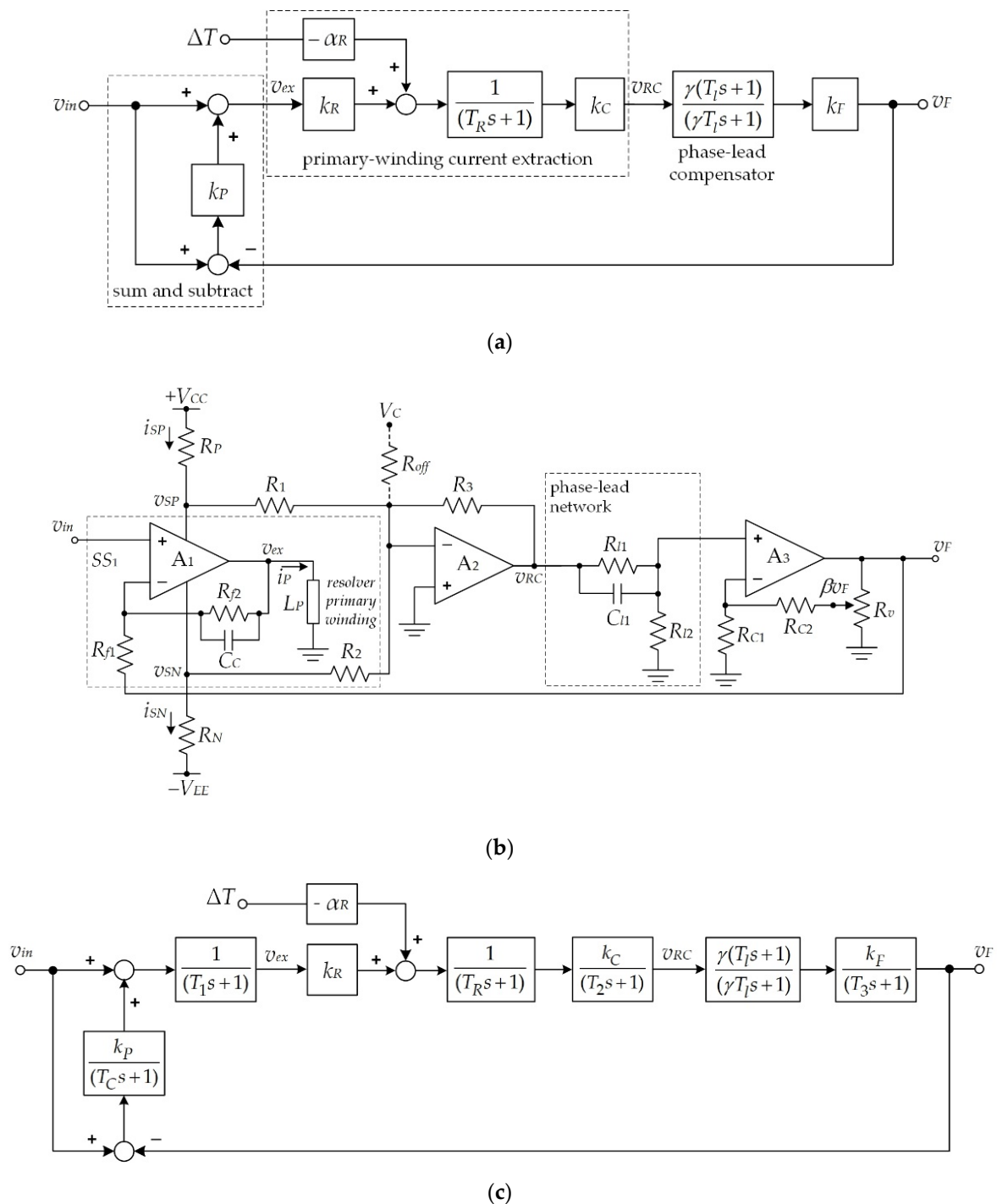


Figure 4. (a) Principle of the temperature-compensation technique; (b) the proposed circuit; (c) block diagram of the proposed circuit.

Notably, the signal v_{ex} is provided as the excitation signal for the resolver. From Equation (18), the signal v_{ex} is in sum-and-subtract form, corresponding to the sum-and-subtract topology in Figure 4a. The primary winding current i_P is detected by the resistors R_P and R_N in the form of voltage signals v_{SP} and v_{SN} , respectively. Opamp A_2 forms the inverting amplifier to obtain the signal v_{RC} from the v_{SP} and v_{SN} signals. The phase-lead compensator formed by capacitor C_{I1} and resistors R_{I1} and R_{I2} provides the phase lead θ_L to compensate for the phase lag θ_P caused by the behavior of the resolver. Opamp A_3 , the resistors R_{C1} and R_{C2} , and the variable resistor R_V provide the compensation gain k_F for

the phase-lead compensator. The relationship between the voltage signals v_{RC} and v_F in Figure 4b for $R_{C1} = R_{C2}$ can be expressed as

$$\frac{v_F(s)}{v_{RC}(s)} = \frac{2\left(s + \frac{1}{T_I}\right)}{\beta\left(s + \frac{1}{\gamma T_I}\right)} = \frac{\gamma k_F(T_I s + 1)}{(\gamma T_I s + 1)} \quad (19)$$

where $\gamma = R_{I2}/(R_{I1} + R_{I2})$ is an attenuation factor, $k_F = 2/\beta$ is a compensation factor, and $T_I = R_{I1}C_{I1}$. The compensation factor k_F is set to $1/\gamma$ for $|v_F(j\omega)| = |v_{RC}(j\omega)|$. Notably, the pole at $s = -1/\gamma T_I$ must be far from the left of the zero at $s = -1/T_I$ to prevent phase error at the excitation frequency. Therefore, the factor $\gamma \leq 0.1$ is chosen to assign the location of the pole shifted left from the location of the 0 by at least 1 decade. The phase lead θ_L in Equation (19) can be stated as

$$\theta_L = \tan^{-1}(\omega_{ex}T_I) - \tan^{-1}(\gamma\omega_{ex}T_I) \quad (20)$$

If $\theta_L = |\theta_P|$ is set, then the voltage signal v_F and the input signal v_{in} are in phase.

4. Performance Analysis

In practical implementation, a deviation from the ideal performance is caused by the non-ideal characteristic of the devices used in the proposed circuit. The tolerances of the resistors and non-identical supply currents of opamp A_1 , i_{SP} , and i_{SN} contribute to the amplitude error and the DC offset voltage in the v_{RC} and v_F signals. The feedback signal v_F , which includes error due to the non-ideal characteristic of the devices used in the circuit in Figure 4b, can be written as

$$v_F = \frac{\gamma 2R_3R_{C2}R_P}{\beta R_1R_{C1}}(1 + \varepsilon_1)i_P + V_{offset} \quad (21)$$

for

$$\varepsilon_1 = \delta_A + \delta_R$$

and

$$V_{offset} = \frac{\gamma 2R_3R_{C2}R_P(\Delta_B + \Delta_S)}{\beta R_1R_{C1}}$$

where δ_A and δ_R are the tolerances of the resistors R_1 , and R_P , respectively; Δ_B and Δ_S are the different currents of the quiescent currents ($I_{B1} - I_{B2}$) and the bias currents of the class-AB output state ($I_{S1} - I_{S2}$) of the opamp A_1 , respectively; and V_{offset} is a DC offset voltage. Practically, the resistances in Equation (21) are set to $R_{C1} = R_{C2}$, $R_P = 500 \Omega$, $R_1 = 10 \text{ k}\Omega$, and $R_3 = 322.7 \text{ k}\Omega$, which were chosen for the tolerance of 0.1% or $\delta_A = \delta_R = 0.001$. From Equation (21), the error ε_1 can be calculated as 2×10^{-3} . The effect of the error ε_1 can be minimized by tuning the compensation factor $k_F = 2/\beta$. The different currents Δ_B and Δ_S are measured from opamp A_1 as about 3.8 and 2.1 μA , respectively. Therefore, the offset voltage V_{offset} can be calculated as 95.2 mV for $k_F = 1/\gamma$. The offset voltage V_{offset} can be cancelled by adjusting the voltage V_C in Figure 4b to an appropriate value. The tolerance of the resistors in the proposed circuit also induces harmonic distortion in the feedback signal v_F for the amplitude of the primary winding current i_P varying in the range of $\pm 2I_S$. The total harmonic distortion (THD) as a percentage of the feedback signal v_F for $-2I_S \leq i_P \leq 2I_S$ can be expressed as

$$\text{THD} = \frac{(\delta_A + \delta_R + \delta_S)i_P}{16\left(1 + \frac{\delta_A + \delta_R}{2}\right)I_S} \times 100\% \quad (22)$$

where $\delta_S = \Delta_S/I_S$. From Equation (22), the maximum percentage of THD occurs when the amplitude of the primary winding current $|i_P|$ is equal to $2I_S$. If the class-AB bias current I_S of opamp A_1 is 1.302 mA, then the THD percentage will be about 0.09%. Notably, the

effect of THD can be prevented. The second factor is the unstable operation of the proposed circuit caused by intermodulation distortion (IMD) and phase shift due to the behavior of the opamps. IMD occurs on the v_{ex} signal due to the intrinsic pole of the opamp A_1 . To avoid IMD, a capacitance C_C is connected in parallel to the resistance R_{f2} to generate the dominant pole for the sum-and-subtract SS_1 . The dynamic behavior of the opamps A_1 , A_2 , and A_3 , caused by the gain bandwidth product (GBP) and the gains k_P and k_F , introduces a phase shift in the feedback signal v_F . Figure 4c shows a block diagram of the proposed circuit where the dynamic behaviors of the opamps are depicted. The time constants T_1 , T_2 , and T_3 of the opamps A_1 , A_2 , and A_3 , respectively, depend on the amplification gains and GBPs of each opamp. From Figure 4b, the time constant $T_C = R_{f2}C_C$ is obtained. In addition, the corner frequency ω_C of the term $(T_Cs + 1)^{-1}$ should be assigned in the range of $10\omega_{ex} \leq \omega_C \leq 0.1GBP_1$ to avoid the unstable operation of the proposed scheme. Practically, the time constant $T_C = (0.1GBP_1)^{-1}$ is assigned. The time constant $T_l = T_R$ is provided to compensate for the phase lag of the primary winding in the resolver structure. The time constants T_1 , T_2 , and T_3 can be stated as

$$T_1 = \frac{(1 + k_P)}{GBP_1} \quad (23)$$

$$T_2 = \frac{(1 + k_C)}{GBP_2} \quad (24)$$

and

$$T_3 = \frac{(1 + k_F)}{GBP_3} \quad (25)$$

where GBP_i is the gain bandwidth product of opamp A_i used in this paper. From Equations (23)–(25), the time constants T_1 , T_2 , and T_3 are proportional to the value of the gains k_P , k_C , and k_F , respectively. Notably, a high value of k_P is used to minimize the temperature effect. In addition, high values of k_P and k_F cause the proposed scheme to operate unstably. The phase shift caused by the pole at $s = -1/T_1$ should approach 0° at the excitation frequency ω_{ex} to avoid unstable operation. Therefore, the time constant T_1 is assigned to be less than at least 1 decade for the period of the excitation frequency ω_{ex} or $T_1 \leq 1/10\omega_{ex}$. From Equation (19), the pole at $s = -1/\gamma T_l$ of the phase-lead compensator should be placed to the left of the 0 at $s = -1/T_l$ by more than 1 decade by adjusting the factor γ to prevent phase error. Therefore, the maximum values of the amplification factors k_P and k_F for maintaining the stable operation of the proposed technique can be expressed as

$$k_P = \frac{GBP_1}{10\omega_{ex}} - 1 \quad (26)$$

and

$$k_F = \frac{GBP_3}{10\omega_{ex}} - 1 \quad (27)$$

From Equations (26) and (27), the maximum value of k_P and k_F for the stability condition is 132.33 for $\omega_{ex} = 18.85$ krad/s $GBP_1 = GBP_2 = GBP_3 = 25.13$ Mrad/s. From Equations (23) and (25), the time constants T_1 and T_3 are calculated as 4.02 and 0.44 μ s for $k_P = 100$ and $k_F = 10$, respectively. The compensated gain k_C is set to 32.27. Therefore, the time constant T_2 can be determined from Equation (24) as 1.32 μ s. From Figure 4b, the resistances R_{f1} and R_{f2} are assigned as 2 and 200 k Ω for the proportional gain $k_P = 100$, respectively. If the time constant $T_C = R_{f2}C_C$ is set to $0.1GBP_1$, about 0.4 μ s, then the capacitance C_C can be determined as 1.99 pF. The phase shifts θ_1 , θ_2 , and θ_3 of the poles at $s = -1/T_1$, $s = -1/T_2$, and $s = -1/T_3$, respectively, can be described by

$$\theta_1 = -\tan^{-1} \left[\frac{\omega_{ex}(1 + k_P)}{GBP_1} \right] \quad (28)$$

$$\theta_2 = -\tan^{-1} \left[\frac{\omega_{ex}(1 + k_C)}{GBP_2} \right] \quad (29)$$

and

$$\theta_3 = -\tan^{-1} \left[\frac{\omega_{ex}(1+k_F)}{GBP_3} \right] \quad (30)$$

For $k_P = 100$, $k_F = 10$, and $k_C = 32.27$, the phases θ_1 , θ_2 , and θ_3 are -4.33° , -1.43° , and -0.47° , respectively. These phase shifts deteriorate the stability of the proposed technique but can be compensated by increasing the phase θ_L of the phase-lead compensator. Therefore, the time constant T_l of the phase-lead compensator can be written as

$$T_l = \frac{\tan(|\theta_P| + |\theta_1| + |\theta_2| + |\theta_3|)}{\omega_{ex}} \quad (31)$$

For $\theta_P = -51.89^\circ$, the time constant T_l can be determined as $85.3 \mu\text{s}$.

In addition, the temperature effect causes deviation of the winding inductance, which is exhibited in the phase shift term φ_D in the primary winding current. The phase shift φ_D can be approximated by the first-order pole at $s = -1/T_D$, where $T_D = (\tan \varphi_D)/\omega_{ex}$. The effect of phase shift φ_D in the time constant T_D can be included in Equation (17) as

$$|v_F(j\omega)| = \left(V_P - \frac{\alpha_R}{k_P} \Delta T \right) \left[\frac{1}{\sqrt{\left(1 + \left(\frac{(\gamma T_l + T_D)\omega_{ex}}{k_P} \right)^2 \right)}} \right] \quad (32)$$

Practically, the time constant T_D is much less than the time constant γT_l and can be omitted. From Equation (32), the denominator of the term in the square brackets can be approximated as 1, corresponding to Equation (17). Therefore, the performance of the proposed scheme is unaffected by the phase shift φ_D .

5. Experimental Results

The proposed technique was implemented using commercially available devices. The opamps used in this study were LF351 for opamp A_1 and LF353, comprising two opamps in the same package for opamps A_2 and A_3 , where LF351 and LF353 provide a GBP of 25.13 Mrad/s . The measured average values of the currents I_B , I_S , Δ_B , and Δ_S for opamp A_1 were 2.39 mA , 1.3 mA , $3.8 \mu\text{A}$, and $2.1 \mu\text{A}$, respectively. The passive devices were chosen as $R_1 = R_2 = 10 \text{ k}\Omega$, $R_{C1} = R_{C2} = 30 \text{ k}\Omega$, $R_{j2} = 200 \text{ k}\Omega$, $R_{j1} = 2 \text{ k}\Omega$, $R_P = R_N = 500 \Omega$, $C_C = 2 \text{ pF}$, and a variable resistor $R_v = 1 \text{ k}\Omega$. All resistors used in the proposed circuit were selected for having a tolerance of 0.1% . The power supply was set to $\pm 12 \text{ V}$. The resolver used to demonstrate the performance of the proposed technique was a SANYO 101-4100 with a transformation factor k_{RS} of 0.37 . The excitation signal was assigned as a 3 kHz sinusoidal wave with 2 V peak amplitude. The load resistors R_{L1} and R_{L2} for the resolver were assigned as $100 \text{ k}\Omega$. The impedance of the resolver including the impedance of the secondary side referred to the primary side was measured from the primary winding using a HIOKI 3532-50 LCR meter as $16.135 \text{ k}\Omega$ at room temperature (25°C). Therefore, the conversion factor k_R was determined as $61.977 \times 10^{-6} \text{ A/V}$. From Equation (13), the factor $k_C = 1/k_R = 16.135 \times 10^3 \text{ V/A}$ was set. Therefore, the resistor R_3 of Equation (13) was determined as $322.7 \text{ k}\Omega$ for $R_N = R_P = 500 \Omega$ and R_1 and $R_2 = 10 \text{ k}\Omega$. The variable resistor was used for the resistor R_3 to achieve $322.7 \text{ k}\Omega$. The circuit in Figure 2b was used to determine the dynamic behavior of the resolver.

Figure 5 shows the measured result of the phase shift between the signal v_{in} and the primary winding current represented by the signal v_{RC} . From Figure 5, the phase lag θ_P between signal v_{in} and signal v_{RC} was measured as 51.98° at a room temperature of 25°C . Therefore, the primary winding impedance including the impedance of the secondary side referred from the primary side can be provided in polar form as $16.135 \text{ k}\Omega \angle -51.98^\circ$. The time constant T_R representing the dynamic behavior of the circuit in Figure 2b was calculated from Equation (14) as $67.63 \mu\text{s}$. From Figure 4b, the time constant $T_l = T_R$ was

assigned to compensate for the phase lag due to the total impedance of the resolver. The attenuation factor $\gamma = 0.1$ was chosen in this experiment. Subsequently, $\gamma T_l = 676 \mu\text{s}$ was obtained. The resistances R_{l1} and R_{l2} were determined as $6.76 \text{ k}\Omega$ and 676Ω , respectively, for $C_{l1} = 0.01 \mu\text{F}$. In this experiment, the resistances R_{l1} and R_{l2} were chosen as 6.8 k and 680Ω , respectively. Therefore, the attenuation factor γ was recalculated as 0.09 . The feedback gain k_F was determined as 11.11 by adjusting the variable resistor R_v . The operation environment of the resolver in this experiment was a chamber capable of varying the temperature from 25 to $70 \text{ }^\circ\text{C}$. The shaft angle θ_S of the resolver was set to 45° to obtain equal amplitudes of the secondary winding signals v_{S1} and v_{S2} . The experimental setup and the prototype of the proposed circuit in Figure 4b are shown in Figure 6a and Figure 6b, respectively.

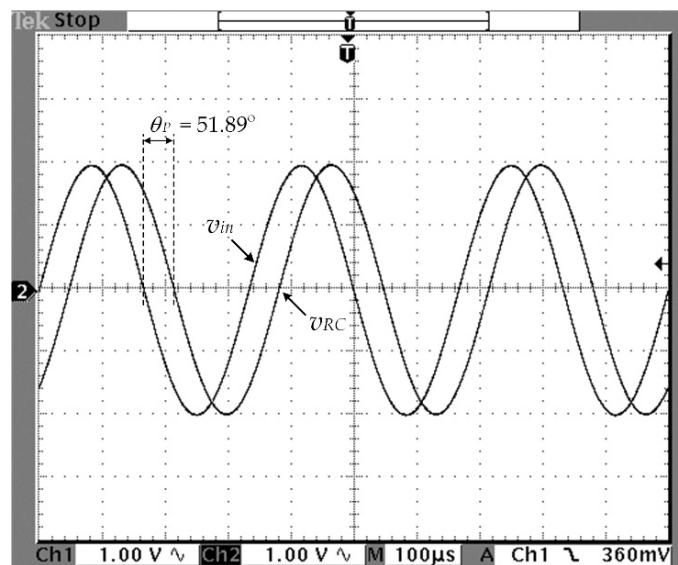


Figure 5. Measured result of signals v_{RC} and v_{in} .

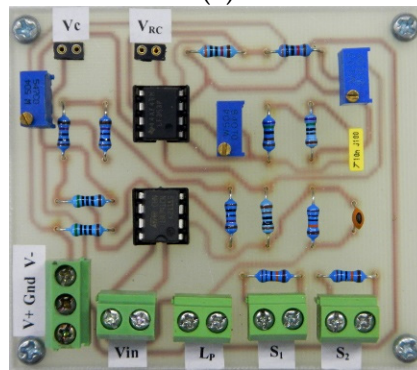
If phase θ_P of the primary winding current at $25 \text{ }^\circ\text{C}$ is set as a phase reference, the phase shift φ_D of the primary winding current shift from the phase reference θ_P can be seen in Figure 7 for the variations in the ambient temperature from 25 to $70 \text{ }^\circ\text{C}$. From Figure 7, the maximum value of the phase shift φ_D at $70 \text{ }^\circ\text{C}$ is about 1.78° , which corresponds to the time constant $T_D = 1.649 \mu\text{s}$. The time constant $\gamma T_l = 676 \mu\text{s}$ is much larger than the time constant T_D . Notably, the effect of the phase shift φ_D on the circuit performance is insignificant and can be neglected.

The phase shift φ_D can be inferred from the change in the resolver inductance. From Figure 7, the variation in the ambient temperature had little influence on the winding inductance of the resolver, in agreement with a recently reported approach [25]. The measured result of the primary winding current in Figure 2a, represented by the signal v_{RC} versus the variation in the ambient temperature, is shown in Figure 8a, which was used to determine the temperature coefficient α of the resolver. The temperature coefficient α of the resolver in the term of α_R was approximated from the signal v_{RC} as $-1.71 \text{ mV}/^\circ\text{C}$ for a 2 V peak amplitude of the excitation signal. The temperature effect on the secondary winding signals v_{S1} and v_{S2} was also measured as shown in Figure 8b. The percentage error for this experimental result can be described as

$$\text{percentage error} = \frac{|\text{expected value} - \text{measured value}|}{\text{expected value}} \times 100\% \quad (33)$$



(a)



(b)

Figure 6. (a) Experimental setup; (b) prototype of the proposed circuit.

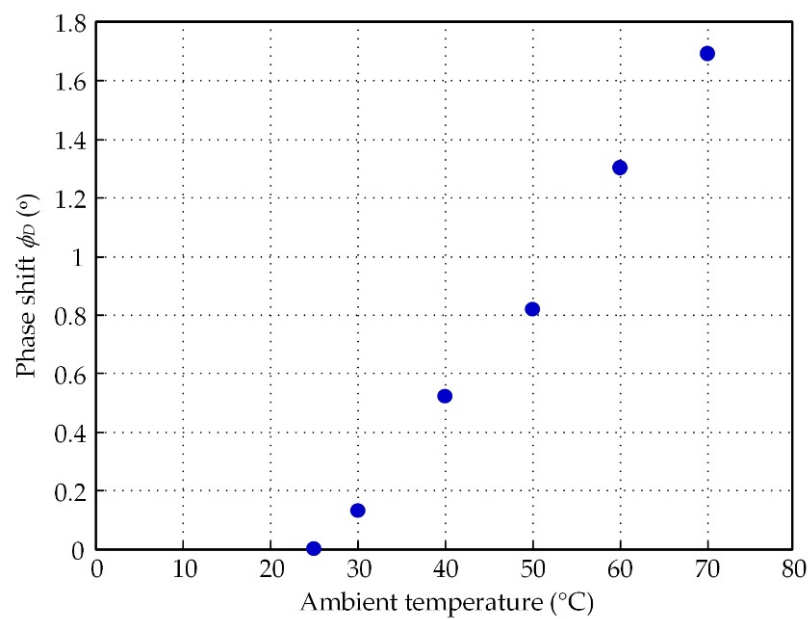


Figure 7. Measured result of phase shift ϕ_D .

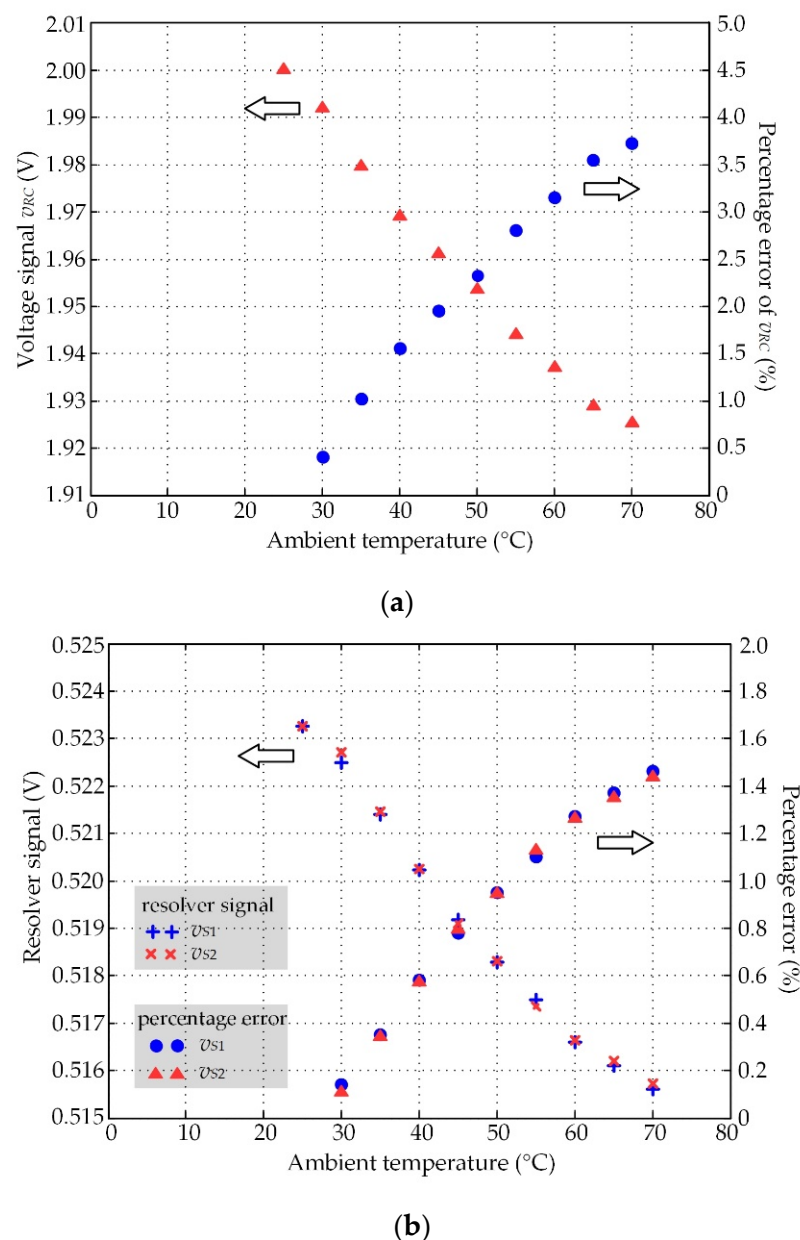
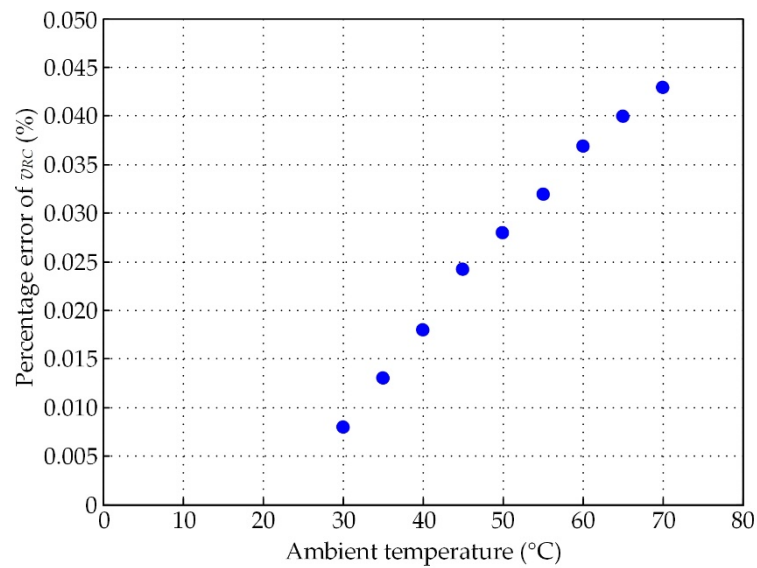


Figure 8. Measured results and percentage errors of resolver signals; (a) voltage signal v_{RC} ; (b) resolver signals v_{S1} and v_{S2} .

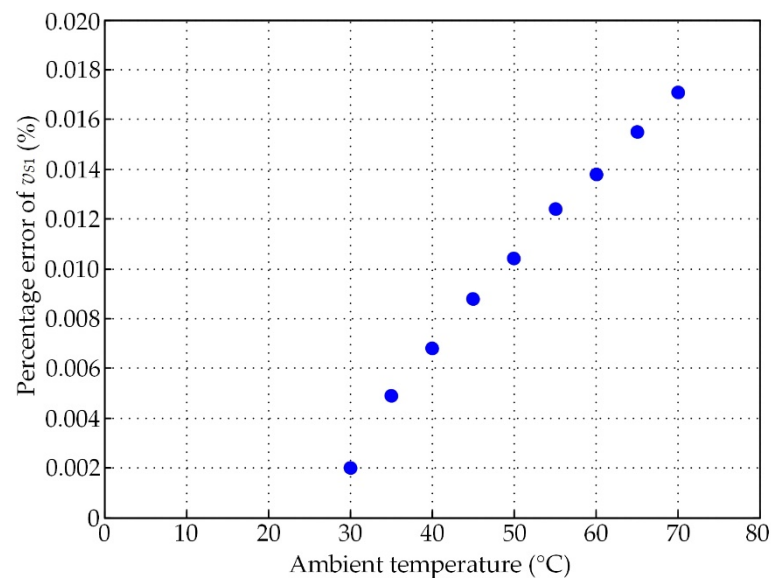
As shown in Figure 8a,b, the magnitude of signals v_{RC} , v_{S1} , and v_{S2} decreased with increasing ambient temperature. The percentage errors at 70 °C of the signals v_{RC} , v_{S1} , and v_{S2} were 3.728%, 1.463%, and 1.44%, respectively. These errors are too high for precision control systems. Therefore, the resolvers require temperature compensation. From Figure 8b, the effect of temperature variation on the resolver signal v_{S2} was the same as on the resolver signal v_{S1} . Therefore, only the resolver signal v_{S1} was used to demonstrate the performance of the proposed technique.

The prototype board in Figure 6b was connected to the resolver for the investigation of the circuit's performance, where the operation environment of the resolver was the same as in the above-described experiment. The experimental results for both signals v_{RC} and v_{S1} in terms of percentage error are provided in Figure 9a,b, respectively. Figure 9a,b show that the errors of the signal v_{RC} and the resolver signals were significantly reduced. Figure 9c depicts the waveform of the excitation signal v_{ex} and the signal v_F for an ambient temperature of 70 °C. The signals v_{ex} and v_F were in phase. From Equation (32), the time

constant T_D was weighted by the proportional gain k_P . Therefore, the performance of the proposed circuit was independent of the time constant T_D or the phase shift φ_D . As shown in Figures 8a and 9a, the percentage error of the primary winding current represented by the signal v_{RC} could be minimized from 3.728% to 0.043% at 70 °C. Additionally, the percentage errors of the resolver signal v_{S1} in Figures 8b and 9b could be reduced from 1.463% to 0.017%. Obviously, the accuracy of the resolver was improved more than 100-fold using the proposed technique. These experimental results confirm that the proposed circuit provides high-quality performance and offers advantages due to a small and simple circuit configuration. In addition, the proposed circuit can be placed between the resolver and a commercial signal conditioner without disturbing the operation of the system.

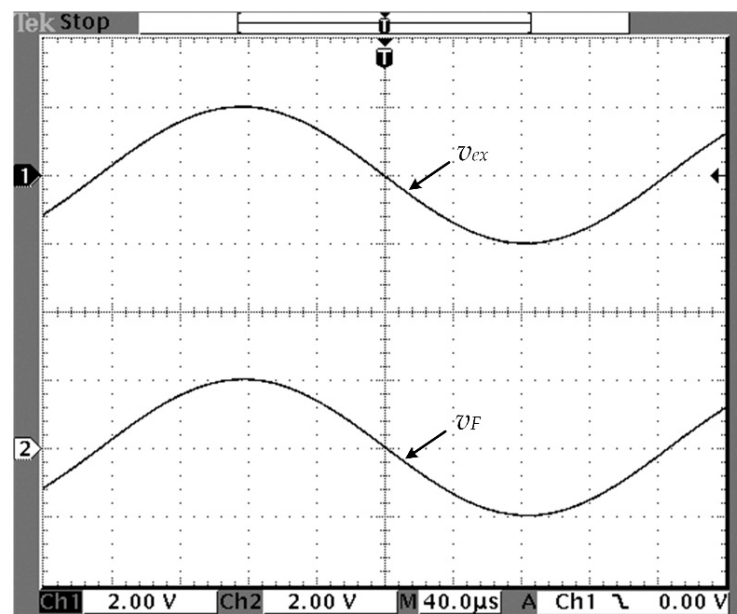


(a)



(b)

Figure 9. Cont.



(c)

Figure 9. Percentage errors of resolver signals with temperature compensation using the proposed technique: (a) voltage signal v_{RC} ; (b) resolver signal v_{S1} ; (c) waveform of signals v_{ex} and v_F .

Author Contributions: Conceptualization, V.R.; methodology, W.P. and A.R.; validation, V.R., W.P., K.S. and A.R.; writing—original draft preparation, W.P.; writing—review and editing, W.P. and A.R.; visualization, K.S. and A.R.; supervision, V.R. All authors have read and agreed to the published version of the manuscript.

Funding: This research received no external funding.

Institutional Review Board Statement: Not applicable.

Informed Consent Statement: Not applicable.

Data Availability Statement: Not applicable.

Conflicts of Interest: The authors declare no conflict of interest.

References

- Pallas-Areny, R.; Webster, J.G. *Sensor and Signal Condition*, 2nd ed.; John Wiley & Sons: New York, NY, USA, 2001; ISBN 0-471-33232-1.
- Figueiredo, J. Resolver Models for Manufacturing. *IEEE Trans. Ind. Electron.* **2011**, *58*, 3693–3700. [\[CrossRef\]](#)
- Petchmaneelumka, W.; Mano, P.; Songsuwankit, K.; Riewruja, V. High Accuracy Resolver-to-Linear Signal Converter. *Int. J. Electron.* **2018**, *105*, 1520–1534. [\[CrossRef\]](#)
- Datlinger, C.; Hirz, M. Benchmark of Rotor Position Sensor Technologies for Application in Automotive Electric Drive Trains. *Electronics* **2020**, *9*, 1063. [\[CrossRef\]](#)
- Attaianese, C.; Tomasso, G. Position Measurement in Industrial Drives by Means of Low-cost Resolver-to-digital Converter. *IEEE Trans. Instrum. Meas.* **2007**, *56*, 2155–2159. [\[CrossRef\]](#)
- Li, Q.; Ding, F. Novel Displacement Eddy Current Sensor with Temperature Compensation for Electrohydraulic Valves. *Sens. Actuators A* **2005**, *122*, 83–87. [\[CrossRef\]](#)
- Sun, L.; Taylor, J.; Guo, X.; Cheng, M.; Emadi, A. A Linear Position Measurement Scheme for Long-Distance and High-Speed Applications. *IEEE Trans. Ind. Electron.* **2021**, *68*, 4435–4447. [\[CrossRef\]](#)
- Cetinkunt, S. *Mechatronics*; John Wiley & Sons: New York, NY, USA, 2006; ISBN 978-0-471-47987-1.
- Casanella, R.; Casas, O.; Pallas-Areny, R. Differential Synchronous Demodulator for Modulating, Sensors and Impedance Measurements. *Meas. Sci. Tech.* **2005**, *16*, 1637–1643. [\[CrossRef\]](#)
- Koukourlis, C.S.; Trigonidis, V.K.; Sahalos, J.N. Differential Synchronous Demodulation for Small-signal Amplitude Estimation. *IEEE Trans. Instrum. Meas.* **1993**, *42*, 926–931. [\[CrossRef\]](#)
- Petchmaneelumka, W.; Songsuwankit, K.; Riewruja, V. Accurate LVDT Signal Converter. *Int. Rev. Electr. Eng.-I* **2016**, *11*, 340–347. [\[CrossRef\]](#)

12. Tongcharoen, J.; Petchmaneelumka, W.; Riewruja, V. Low-Cost Resolver-to-DC Converter. In Proceedings of the 15th International Conference on Control, Automation and Systems, Busan, Korea, 13–16 October 2015; pp. 1699–1702. [[CrossRef](#)]
13. Wang, Y.; Zhu, Z.; Zuo, Z. A Novel Design Method for Resolver-to-digital Conversion. *IEEE Trans. Ind. Electron.* **2015**, *62*, 3724–3731. [[CrossRef](#)]
14. Shi, T.; Hao, Y.; Jiang, G.; Wang, Z.; Xia, C. A Method of Resolver-to-Digital Conversion Based on Square Wave Excitation. *IEEE Trans. Ind. Electron.* **2018**, *65*, 7211–7219. [[CrossRef](#)]
15. Wang, K.; Wu, Z. Oversampling Synchronous Envelope Detection for Resolver-to-Digital Conversion. *IEEE Trans. Ind. Electron.* **2020**, *67*, 4867–4876. [[CrossRef](#)]
16. Qin, H.; Wu, Z. Angle Tracking Observer with Improved Accuracy for Resolver-to-Digital Conversion. *Symmetry* **2019**, *11*, 1347. [[CrossRef](#)]
17. Estrabis, T.; Gentil, G.; Cordero, R. Development of a Resolver-to-Digital Converter Based on Second-Order Difference Generalized Predictive Control. *Energies* **2021**, *14*, 459. [[CrossRef](#)]
18. Hwang, S.H.; Kim, H.J.; Kim, J.M.; Liu, L.; Li, H. Compensation of Amplitude Imbalance and Imperfect Quadrature in Resolver Signals for PMSM Drives. *IEEE Trans. Ind. Appl.* **2011**, *47*, 134–143. [[CrossRef](#)]
19. Strayer, L.R.; Lutton, M.D.; Begley, C.C. Temperature Compensation of an Inductive Sensor. U.S. Patent 2003/0052696A1, 20 March 2003.
20. Zheng, S.; Wang, Y.; Ren, H. Simultaneous Temperature Compensation and Synchronous Error Elimination for Axial Displacement Sensors Using an Auxiliary Probe. *IEEE Trans. Ind. Electron.* **2016**, *63*, 3179–3186. [[CrossRef](#)]
21. Wang, H.; Ju, B.; Li, W.; Feng, Z. Ultrastable Eddy Current Displacement Sensor Working in Harsh Temperature Environments with Comprehensive Self-temperature Compensation. *Sens. Actuators A* **2014**, *211*, 98–104. [[CrossRef](#)]
22. Lv, Y.T.; Zhu, C.S. High temperature eddy current displacement sensor based on temperature drift compensation. *J. Zhejiang Univ. (Eng. Sci.)* **2015**, *4*, 749–753.
23. Grima, A.; Castro, M.D.; Masi, A.; Sammut, N. Design Enhancements of an Ironless Inductive Position Sensor. *IEEE Trans. Instrum. Meas.* **2020**, *69*, 1362–1369. [[CrossRef](#)]
24. Wu, L.; Zhao, G.; Ying, J.; Feng, Z. A Thermal Drift Compensation Method for Precision Sensors Considering Historical Temperature State. *IEEE Trans. Ind. Electron.* **2021**, *68*. [[CrossRef](#)]
25. Zhao, Z.; Liu, Z.; Lyu, Y.; Gao, Y. Experimental Investigation of High Temperature-Resistant Inductive Sensor for Blade Tip Clearance Measurement. *Sensors* **2019**, *19*, 61. [[CrossRef](#)] [[PubMed](#)]
26. Wang, H.B.; Feng, Z.H. Ultrastable and highly sensitive eddy current displacement sensor using self-temperature compensation. *Sens. Actuators A* **2013**, *203*, 362–368. [[CrossRef](#)]
27. Petchmaneelumka, W.; Rerkratn, A.; Luangpol, A.; Riewruja, V. Compensation of Temperature Effect for LVDT Transducer. *J. Circuit Syst. Comp.* **2018**, *27*, 1850182. [[CrossRef](#)]
28. Melkebeek, J.A. *Electrical Machines and Drives: Fundamentals and Advanced Modelling*; Springer: Cham, Switzerland, 2018; ISBN 978-3-319-72730-1.
29. Riewruja, V.; Kamsri, T. Square-rooting and Absolute Function Circuits using Operational Amplifiers. *IET Circuits Devices Syst.* **2009**, *3*, 57–63. [[CrossRef](#)]
30. Riewruja, V.; Rerkratn, A. Analog Multiplier using Operational Amplifier. *Indian J. Pure Appl. Phys.* **2010**, *48*, 67–70.
31. Riewruja, V.; Rerkratn, A. Four-quadrant Analogue Multiplier using Operational Amplifier. *Int. J. Electron.* **2011**, *98*, 459–474. [[CrossRef](#)]
32. Nasir, B.A. An Accurate Iron Core Loss Model in Equivalent Circuit of Induction Machines. *J. Energy* **2020**, *2020*, 7613737. [[CrossRef](#)]